2014-04

Optical Architecture Design for Detection of Absorbers Embedded in Visceral Fat

UTD AUTHOR(S): Robert Francis, James Florence and Duncan L. MacFarlane

Optical architecture design for detection of absorbers embedded in visceral fat

Robert Francis,[1,2,*] James Florence,[1,2] and Duncan MacFarlane[2]

[1] *Raytheon EO Innovations, 1601 N Plano Rd, Richardson, TX 75081, USA*
[2]*Department of Electrical Engineering, University of Texas Dallas, 800 W Campbell Rd, Richardson, TX 75080, USA*
[*]*Robert.francis@raytheon.com*

Abstract: Optically absorbing ducts embedded in scattering adipose tissue can be injured during laparoscopic surgery. Non-sequential simulations and theoretical analysis compare optical system configurations for detecting these absorbers. For absorbers in deep scattering volumes, trans-illumination is preferred instead of diffuse reflectance. For improved contrast, a scanning source with a large area detector is preferred instead of a large area source with a pixelated detector.

OCIS codes: (110.0113) Imaging through turbid media; (170.0110) Imaging systems.

References and links

1. Z. B. Ou, S. W. Li, C. A. Liu, B. Tu, C. X. Wu, X. Ding, Z. J. Liu, K. Sun, H. Y. Feng, and J. P. Gong, "Prevention of common bile duct injury during laparoscopic cholecystectomy," HBPD INT **8**(4), 414–417 (2009).
2. H. Akbari, Y. Kosugi, and Z. Khorgami, "Image-guided preparation of the calot's triangle in laparoscopic cholecystectomy," in *Proceedings of EMBS EMBC Annual International Conference of the IEEE* (2009).
3. S. J. Savader, K. D. Lillemoe, C. A. Prescott, A. B. Winick, A. C. Venbrux, G. B. Lund, S. E. Mitchell, J. L. Cameron, and F. A. Osterman, Jr., "Laparoscopic cholecystectomy-related bile duct injuries: A health and financial disaster," Ann. Surg. **225**(3), 268–273 (1997).
4. A. R. Moossa, D. W. Easter, E. Van Sonnenberg, G. Casola, and H. D'Agostino, "Laparoscopic injuries to the bile duct. A cause for concern," Ann. Surg. **215**(3), 203–208 (1992).
5. M. T. Perera, M. A. Silva, A. J. Shah, R. Hardstaff, S. R. Bramhall, J. Issac, J. A. Buckels, and D. F. Mirza, "Risk factors for litigation following major transectional bile duct injury sustained at laparoscopic cholecystectomy," World J. Surg. **34**(11), 2635–2641 (2010).
6. A. C. Medeiros, I. Araújo-Filho, M. D. F. Carvalho, M. de Paiva, V. F. Lima, I. M. de Azevedo, and A. M. Dantas Filho, "Laparoscopic versus open cholecystectomy: Complications and cost," J. Surg. Clin. Res. **3**, 49–58 (2013).
7. O. J. Garden, "Fluorescent cholangiography illuminating the biliary tree during laparoscopic cholecystectomy," Br. J. Surg. **97**(9), 1378 (2010).
8. F. Xu, C. G. Xu, and D. Z. Xu, "A new method of preventing bile duct injury in laparoscopic cholecystectomy," World J. Gastroenterol. **10**(19), 2916–2918 (2004).
9. N. Sato, K. Shibao, Y. Akiyama, Y. Inoue, Y. Mori, N. Minagawa, A. Higure, and K. Yamaguchi, "Routine intraoperative cholangiography during single-incision laparoscopic cholecystectomy: A review of 196 consecutive patients," J. Gastrointest. Surg. **17**(4), 668–674 (2013).
10. M. A. Stott, P. A. Farrands, P. B. Guyer, K. C. Dewbury, J. J. Browning, and R. Sutton, "Ultrasound of the common bile duct in patients undergoing cholecystectomy," J. Clin. Ultrasound **19**(2), 73–76 (1991).
11. V. Salvatore, A. Borghi, and F. Piscaglia, "Contrast-enhanced ultrasound for liver imaging: Recent advances," Curr. Pharm. Des. **18**(15), 2236–2252 (2012).
12. A. N. Bashkatov, E. A. Genina, V. I. Kochubey, and V. V. Tuchin, "Optical properties of human skin, subcutaneous and mucous tissues in the wavelength range from 400 to 2000 nm," J. Phys. D Appl. Phys. **38**(15), 2543–2555 (2005).
13. L. V. Wang and H. Wu, *Biomedical Optics: Principles and Imaging* (Hoboken: Wiley; 2012), Chap. 5.
14. A. H. Hielscher, R. E. Alcouffe, and R. L. Barbour, "Comparison of finite-difference transport and diffusion calculations for photon migration in homogeneous and heterogeneous tissues," Phys. Med. Biol. **43**(5), 1285–1302 (1998).
15. D. Contini, F. Martelli, and G. Zaccanti, "Photon migration through a turbid slab described by a model based on diffusion approximation. I. Theory," Appl. Opt. **36**(19), 4587–4599 (1997).
16. S. Fantini, M. A. Franceschini, and E. Gratton, "Semi-infinite-geometry boundary problem for light migration in highly scattering media: A frequency-domain study in the diffusion approximation," J. Opt. Soc. Am. B. **11**(10), 2128–2138 (1994).

#201719 - $15.00 USD Received 20 Nov 2013; revised 17 Mar 2014; accepted 27 Mar 2014; published 9 Apr 2014

17. T. Tarvainen, M. Vauhkonen, V. Kolehmainen, S. R. Arridge, and J. P. Kaipio, "Coupled radiative transfer equation and diffusion approximation model for photon migration in turbid medium with low-scattering and non-scattering regions," Phys. Med. Biol. **50**(20), 4913–4930 (2005).
18. G. Alexandrakis, T. J. Farrell, and M. S. Patterson, "Monte Carlo diffusion hybrid model for photon migration in a two-layer turbid medium in the frequency domain," Appl. Opt. **39**(13), 2235–2244 (2000).
19. D. A. Boas, M. A. O'Leary, B. Chance, and A. G. Yodh, "Scattering and wavelength transduction of diffuse photon density waves," Phys. Rev. E Stat. Phys. Plasmas Fluids Relat. Interdiscip. Topics **47**(5), R2999–R3002 (1993).
20. M. A. O'Leary, D. A. Boas, B. Chance, and A. G. Yodh, "Refraction of diffuse photon density waves," Phys. Rev. Lett. **69**(18), 2658–2661 (1992).
21. R. Irvin, FRED Technical Support, Photon Engineering, (personal communication, 2014).
22. V. G. Peters, D. R. Wyman, M. S. Patterson, and G. L. Frank, "Optical properties of normal and diseased human breast tissues in the visible and near infrared," Phys. Med. Biol. **35**(9), 1317–1334 (1990).
23. T. L. Troy, D. L. Page, and E. M. Sevick-Muraca, "Optical properties of normal and diseased breast tissues: prognosis for optical mammography," J. Biomed. Opt. **1**(3), 342–355 (1996).
24. P. D. Agrba, M. Y. Kirillin, A. I. Abelevich, E. V. Zagaynova, and V. A. Kamensky, "Compression as a method for increasing the informativity of optical coherence tomography of biotissues," Opt **107**(Spec.), 853–858 (2009).

1. Introduction

Current laparoscopic imaging modalities limit a surgeon's ability to accurately identify the location of critical anatomy if it is embedded in visceral fat. For example, in laparoscopic cholecystectomy there is a risk of injuring the common bile duct (CBD) while attempting to cut the cystic duct, especially if fat obstructs the surgeons view [1,2]. The CBD is between 2 mm and 6 mm in diameter depending on overall body size and can be embedded in up to 20 mm of omental fat. In order to remove the gallbladder a surgeon first exposes and opens Calot's triangle, the region formed by the cystic duct and common hepatic duct just superior to the CBD. Exposure of Calot's triangle requires removal of omental visceral fat by cutting or burning. Eventually, the surgeon should cut the cystic duct intentionally to remove the gallbladder, but while trying to locate the cystic duct, injury to the CBD can occur. Injuring the CBD leads to increased morbidity and recovery time, which adds to the overall cost of healthcare in secondary procedures and increased hospitalization [3–6]. Minimally invasive laparoscopic procedures are guided by cameras inserted a single 10 mm abdominal incision port, which only give a surface view of the fat covering the biliary tree. Current advanced optical imaging modalities cannot image through more than 5 mm of fat or require exogenous contrast agents [7–9]. Non-optical imaging modalities such as ultrasound can see through the fat, but have lower resolution and probes are typically too large for laparoscopic insertion [10,11]. Surgeons need a laparoscopic, non-invasive optical imaging modality which allows them to locate these ducts and other critical anatomy when embedded in fat.

It is helpful in framing the problem to consider the relative absorption and scattering spectra of the various tissue types involved in the imaging task. The water content in gallbladder tissue, bile, and blood is greater than the water content in adipose tissue. Water has an optical absorption peak at 1437 nm, therefore the optical absorption spectra of gallbladder tissue, bile, and blood has a very high peak at 1437 nm relative to a lower peak seen in the optical absorption spectrum of adipose [12]. Fat tissue is highly scattering, even at longer wavelengths, so the problem of locating bile ducts in fat tissue can be abstracted to locating absorbing structures located in scattering media. This paper compares potential imaging system configurations for detecting absorbers embedded in scattering media based on contrast. In particular, a system configuration with a large source and pixelated detector is compared to a small scanned source and large area detector in transmission and reflectance. Analytical modeling, theoretical Monte Carlo simulations and experimental results comprise the basis for this comparison. The analysis is important in order to help select the preferred optical architecture for designing a new laparoscopic instrument.

#201719 - $15.00 USD Received 20 Nov 2013; revised 17 Mar 2014; accepted 27 Mar 2014; published 9 Apr 2014

2. Methods

2.1 Theoretical construction of absorber embedded in scattering media

Imaging through turbid or diffusely scattering media is analyzed for tissue optics by the diffusion approximation solution to the radiative transfer equation (RTE) [13]. This approximation is valid deep in tissue but has errors at interfaces, especially near the source-tissue interface [14–16]. A time-independent, point source solution to the diffusion equation describes intensity by the Green's function in Eq. (1).

$$\phi(r_0) = \frac{1}{4\pi D}\frac{\exp[-\mu_{eff} r_0]}{r_0} \tag{1}$$

D and μ_{eff} are parameters that depend on the absorption coefficient (μ_a) and reduced scattering coefficient (μ_s') of the tissue, where g is the anisotropy constant. D is the diffusion constant defined by Eq. (2), and μ_{eff} is the effective attenuation coefficient defined by Eq. (3) [13].

$$D = \frac{1}{3(\mu_a + \mu_s^{'})} \tag{2}$$

$$\mu_{eff} = \sqrt{3\mu_a(\mu_a + \mu_s^{'})} \tag{3}$$

An extension of this approximation is the solution for a pencil beam incident on the surface of the scattering block, in which the pencil beam is modeled as a point source originating at a depth of $z_s = 1/\mu_s^{'}$ so that $r_0 = \sqrt{(x_a - x_s)^2 + (y_a - y_s)^2 + (z_a - z_s)^2}$ in Eq. (1).

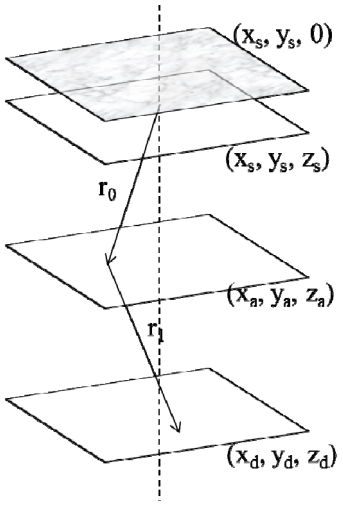

Fig. 1. Planar geometry for describing light propagation where ballistic photons flow from the fat surface (z = 0) to the diffuse point source origin (z = z_s), intensity is described by the Green's function in Eq. (1) for z_s to the aperture plane (z = z_a), and intensity is described by Eq. (4) for z_a to the detector plane (z = z_d).

Equation (1) adequately describes forward propagation of light in a homogenous, infinite block of tissue, but does not comprehend structures with different absorbing and scattering properties embedded in the block. Other studies have shown that the conventional diffusion approximation is inadequate to model scattering material with low-scattering inclusions [17,18]. To comprehend these low-scattering, high-absorbing structures theoretically, the diffusion region is assumed to have a discontinuity at an aperture plane. A Huygen's integral approach similar to the diffraction approach shown by [19,20] is taken based on the geometry

#201719 - $15.00 USD Received 20 Nov 2013; revised 17 Mar 2014; accepted 27 Mar 2014; published 9 Apr 2014

in Fig. 1 where propagation from the source plane to the aperture plane is described by Eq. (1) and the propagation to the detector plane is calculated by integrating each point in the aperture plane as a new source propagated by distance $r_1 = \sqrt{(x_d - x_a)^2 + (y_d - y_a)^2 + (z_d - z_a)^2}$ as in Eq. (4). Numerical integration is performed in this paper to compare the intensity at the detector plane when calculated with Eq. (1) only (no aperture plane) and when calculated with Eq. (4) (integrating over a semi-infinite clear aperture plane). To simulate an absorber in the aperture plane, we multiply the integrand by a transmission function, $\tau(x_a, y_a)$. For a perfect absorber $\tau(x_a, y_a)$ is 0 in the area of the absorber and 1 elsewhere, as written for a flat bar absorber in Eq. (5). The bar absorber is sufficient for modeling optical system configurations but does not account for the shadowing and near-field effects caused by a three-dimensional rod absorber.

$$\phi(x_d, y_d, z_d) = \frac{z_d - z_a}{8\pi^2 D} \iint_{x_a y_a} \tau(x_a, y_a) \frac{e^{-\mu_{eff}(r_1 + r_0)}}{r_0 r_1^3} \left(1 + \mu_{eff} r_1\right) dy dx \tag{4}$$

$$\tau(x_a, y_a) = \begin{cases} 0, & -1 \le x_a \le 1 \\ 1, & |x_a| > 1 \end{cases} \tag{5}$$

2.2 3D Monte Carlo simulation of scattering and absorption in digital phantom

2.2.1 Digital phantom

A digital phantom is created with an absorbing rod, D_A = 2 mm, of a material (U_A) with μ_a = 2.05 mm^{-1} and μ_s = 0.75 mm^{-1} embedded in a 160 mm x 160 mm block of scattering material (U_S) with thickness D_S = 12 mm and μ_a = 0.12 mm^{-1} and μ_s = 0.75 mm^{-1} . In Fig. 2(a) is shown a 2-dimensional cross-section of the 3-dimensional digital phantom. The tissue block lateral dimensions are selected so that no rays exit the sides of the block, and this simulates an infinite block of tissue with a detector plane 12 mm from the front surface. This allows comparison with the analytic model and also describes our experimental situation well. Non-sequential ray-tracing software (FRED, Photon Engineering) is used to simulate different system configurations and compare percent contrast for the rod at different depths in the scattering block. The source is defined as a coherent 1437 nm plane wave comprised of 10,000 starting ray positions (photons) in a 1 mm diameter beam. As each ray propagates through the scattering material, it changes direction (according to the Henyey-Greenstein function with g = 0.9) and power (according to Beer's law) a maximum of 100,000 times and is completely absorbed by a detector if it escapes the top or bottom surface of the scattering block.

A lateral view of example photon propagation paths is shown in Fig. 2(b). The paths are 3D, but viewed from the side in order to illustrate the beam orientation normal to the fat block on Side A. Rays that scatter more than the maximum are considered absorbed by the scattering material. Absorption is calculated in FRED by keeping track of the ray path length between two intersection points, including the path length resulting from multiple volume scatter events. Once the path length is known, the corresponding flux is taken out of the ray's power according to the absorption coefficient of the material [21]. The refractive index of both tissue materials (U_S and U_A) is set to 1.33 and both surfaces of the block are modeled to have a 100% anti-reflective coating so that surface reflections are ignored.

#201719 - $15.00 USD Received 20 Nov 2013; revised 17 Mar 2014; accepted 27 Mar 2014; published 9 Apr 2014

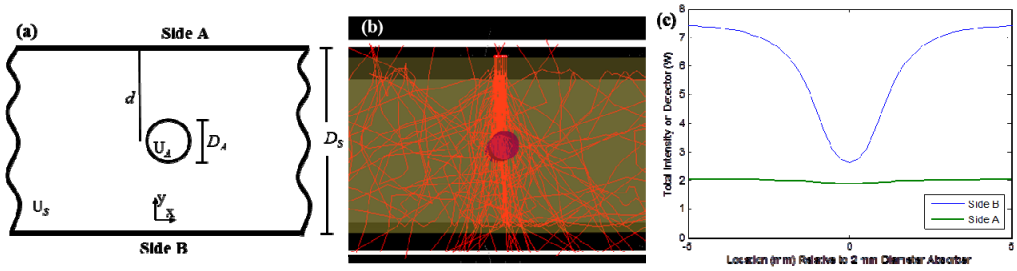

Fig. 2. 2-dimensionalcross-section of the 3-dimensional digital phantom (a); and viewed in FRED (b). The source is scanned linearly across the absorbing rod and at each point in the scan the intensity is captured by a detector on Side B and Side A. Line profiles when d = 5 and source power is 25 W are shown in (c).

2.2.2 Simulated scans and processing methods

The source is on Side A and is scanned in 0.25 mm steps perpendicular to the direction of the absorbing rod. At each step, the ray intensity escaping the top and bottom of the block is counted by a detector on Side A and a detector on Side B. Each of the detectors is 40 mm x 40 mm with 0.25 mm pixel pitch. The total intensity captured on each detector at each point in the scan is then plotted versus the beam location as in Fig. 2(c). Notation for the intensity on each detector depends on the pixel location (x,y) and the source location (x_s,y_s) for Side A, $\Psi_A(x,y,x_S,y_S)$, and for Side B, $\Psi_B(x,y,x_S,y_S)$.

To simulate a diffuse reflectance system, all of the pixels on the Side A detector are summed to represent a single large area detector (LAD) per Eq. (6), effectively replacing the pixelated detector with a single photodiode, where $I_{A,LAD}$ is the intensity on the photodiode. Two processing methods are used in the simulation of a trans-illumination system: LAD and a pixelated detector (PD). The trans-illumination LAD simulation is per Eq. (7), and represents a scanning laser source at position (x_s,y_s) with a single large area photodiode opposite the source, where $I_{B,LAD}$ is the intensity on the photodiode. The trans-illumination PD simulation assumes a large stationary source, so its intensity profile is calculated by summing over all of the scanned source locations per Eq. (8), and the detector is pixelated as in a focal plane array. So, $I_{B,PD}(x,y)$ is the intensity at pixel (x,y) on the focal plane on Side B due to all source positions of the laser on Side A.

$$I_{A,LAD}(x_S,y_S)=\sum_X\sum_Y\Psi_A(x,y,x_S,y_S) \tag{6}$$

$$I_{B,LAD}(x_S,y_S)=\sum_X\sum_Y\Psi_B(x,y,x_S,y_S) \tag{7}$$

$$I_{B,PD}(x,y)=\sum_{X_S}\sum_{Y_S}\Psi_B(x,y,x_S,y_S) \tag{8}$$

Monte Carlo simulations are run for 1 ≤ d ≤ 11 in 1 mm increments and the pixelated detector responses are stored for offline calculation of intensity response (I) in accordance with the above equations. The signal (S) is then calculated as the intensity response at the location of the absorber, ΣI(x = 0,y) for all y, and the background (B) is calculated as the intensity response away from the absorber, ΣI(x = ± 5,y) for all y. Contrast is formulated as C = (B-S)/B so that 1 is perfect contrast and 0 is no contrast.

2.3 Experimental measurements

2.3.1 Fat samples

Omental fat tissue samples excised from human patients undergoing open surgeries were immediately stored in individual containers within a cryogenic freezer at –80° C. Each

#201719 - $15.00 USD Received 20 Nov 2013; revised 17 Mar 2014; accepted 27 Mar 2014; published 9 Apr 2014

sample was from a unique patient and taken with prior written consent from the patient in accordance with UTSW IRB # 072010-187 at University and Parkland Hospitals (Dallas, TX). The samples were stored for 6 to 24 months prior to use in this imaging study, and 16 samples were examined with varying experimental protocols throughout the study. Each sample was thawed in a refrigerator at 5°-10° C for 1 to 7 days before initial use. Frozen and thawed subcutaneous adipose tissue samples have been previously validated as having the same optical properties as freshly harvested samples [22,23]. Omental adipose undergoes similar transformations as subcutaneous adipose during the freeze-thaw cycle, so the results in this paper should not significantly differ from results with fresh omental fat tissue. Results presented in this paper are from the first day of imaging a sample, but it is possible to image a sample on one day, then return it to the refrigerator and use it the next day. However, the color of the fat turns from red to brown after two days of imaging and the absorption increases significantly so that the assumption of the material as a predominant scattering material no longer holds after multiple imaging sessions of the same sample.

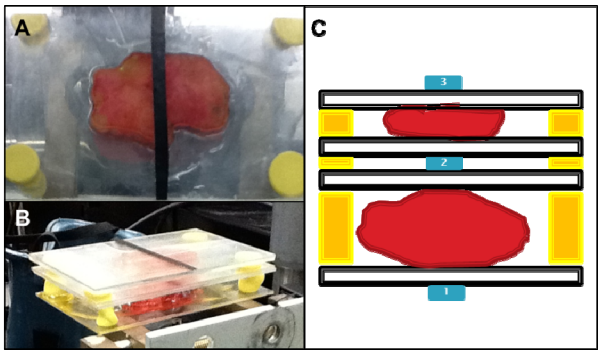

Fig. 3. View of fat sample from Side B (a) and isometric (b). Construction of fat sample sandwich with three locations for inserting and removing an absorber (c).

Noticeable sources of heterogeneity within each sample include spatially varying density of the adipose itself, interstitial fluid, connective tissue, blood vessels, and air pockets. Placing the fat sample into a 20 mm x 10 mm quartz cuvette increased the occurrence of these artifacts, so the preferred method of sample preparation is placing the fat sample on a 2" x 3" glass slide and setting a second glass slide on top of the fat sample. Adhesive spacers are inserted on the corners of the two slides to maintain a fixed sample thickness (yellow parts in Fig. 3). This method of sample preparation compresses the fat somewhat, so the effective optical attenuation of the tissue may be increased [24]. Because of this, sample preparation is inadequate for quantization of in-vivo tissue optical properties, but it is sufficient for making optical system configuration decisions.

A major difference between the digital phantom in Section 2.2 and the experimental fat sample is the glass slides and the air gap between the two sections of fat. To address this difference, a second digital phantom with these features is modelled and analyzed.

2.3.2 Instrument setup and data acquisition

Simulation results lead to the design of a trans-illumination breadboard system for testing with real scattering material. In Lab Setup #1 (Fig. 4), fat tissue samples are imaged with a SWIR camera while illuminated by a scanned 1450 nm collimated, 1 mm, source (Roithner Lasertechnik, L145T600m). The source is manually scanned in a line by adjusting an X-axis micrometer in 150 µm steps through a range of 21 mm. At the end of each line the Y-axis micrometer is adjusted 1.2 mm for multiple line scans. A 640x480 image is captured with an InGaAs SWIR camera (Goodrich, Inc.) through a 50 mm lens at each laser location. For LAD processing, a subset of 200x200 image pixels are summed from each image to represent the response of a single large area detector at each point in the scan. For PD processing, all 640x480 pixels are integrated across all scan locations to represent a larger source.

#201719 - $15.00 USD Received 20 Nov 2013; revised 17 Mar 2014; accepted 27 Mar 2014; published 9 Apr 2014

Lab Setup #1 is used for comparison of processing methods because of the pixelated detector, but it is not fast enough to capture data with higher scan density. Therefore, a second setup is built with a MEMS scan mirror (Mirrorcle Technologies, Inc.) and a single large area photodiode (Newport, Inc.) to facilitate fast, higher density scanning. Lab Setup #2 is limited to only LAD processing because the detector is not pixelated.

In each experiment, the fat thickness for each of the two sections is measured as the distance between the glass slides, and there is a 1 mm air gap in between the two central glass slides for easy insertion and removal of an absorber (Fig. 3(c)). The middle air gap allows capture of control images of the scattering block before and after the absorber is inserted. The absorber can alternatively be placed on the side of the sample closest to the detector or on the side of the sample closest to the source.

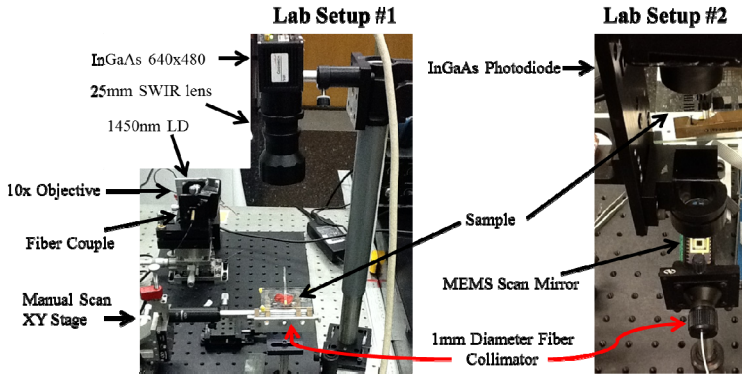

Fig. 4. Photographs of manual scanning setup with pixelated detector (Lab Setup #1) and automatic scanning setup with single large area detector (Lab Setup #2).

3. Results and discussion

3.1 Theoretical and simulation results

The theoretical derivation of intensity calculated by Eq. (4) matches the intensity calculated by Eq. (1) within 0.03 dB, as seen in the line profiles of Fig. 5(a). Discontinuity at the aperture plane causes the largest deviation in Eq. (4) from Eq. (1), even when the transmission function is unity. This deviation is caused by the numerical approximation of the integral in Eq. (4). For these simulations the integral was calculated over 400 x 400 points in a 40 mm x 40 mm aperture plane, and the plotted line profiles are at $x = 0$, $y = 0$.

The diffusion theory approximation of intensity matches the Monte Carlo estimation of intensity, as seen in the line profiles of Fig. 5(b), except for near the surfaces of the fat block and near the plane of the absorber. Discontinuities at the boundaries is expected, since the assumption of infinite depth of scattering material used in the theory approximation is not met in the Monte Carlo simulation.

Signal level is generally higher in trans-illumination compared to diffuse reflectance for a 12 mm thick fat sample, except for when the absorber is close to the source in z and the source is directly over the absorber in x. Comparing Figs. 6(a) and 6(b), the transmitted intensity is ~3.5x the diffusely reflected intensity at x = ± 5, but the intensities are about equal when d = 1mm and x = 0. This contributes to a faster drop in contrast when the detector is on Side A versus when the detector is on Side B as shown in the green line of Fig. 8(d). For lower values of g, the anisotropy factor, the two LAD contrast curves will be in closer agreement.

#201719 - $15.00 USD Received 20 Nov 2013; revised 17 Mar 2014; accepted 27 Mar 2014; published 9 Apr 2014

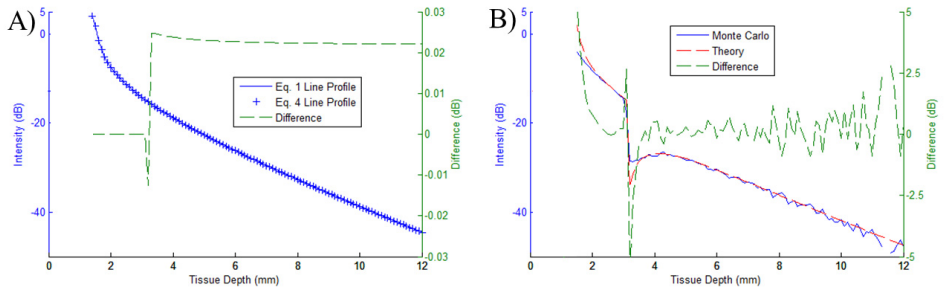

Fig. 5. Line profiles of Eq. (4) compared to Eq. (1) with unity transmission function (a), and line profile of Eq. (4) with bar absorber transmission function compared to cross section of intensity in Monte Carlo simulation (b).

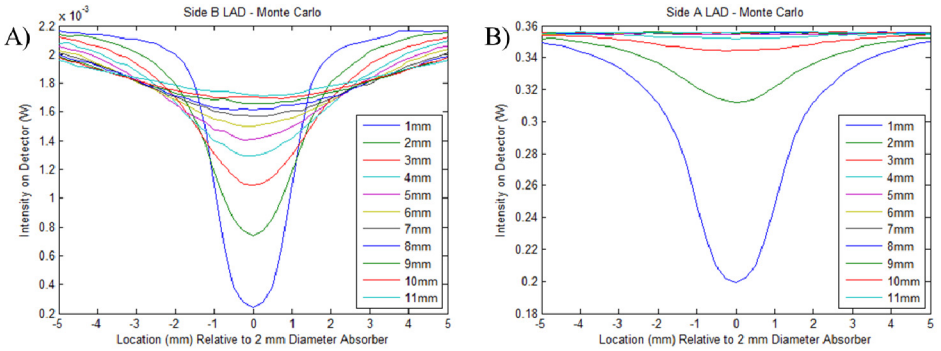

Fig. 6. Line profiles of Eq. (5) for Side B LAD processing (a) compared to line profiles of Eq. (6) for Side A LAD processing (b) based on Monte Carlo simulations with a bar absorber stepped in 1mm increments through a 12 mm block of fat tissue.

Monte Carlo simulations also show that Large Area Detector (LAD) processing has higher contrast than Pixelated Detector (PD) processing when the absorber is at most depths except for when the absorber is closest to the detector. Figure 7(a) shows the line profiles of LAD processing on Side B which indicate that contrast is best when the absorber is closest to Side A and it gradually worsens as the absorber moves toward Side B. This is due to the percent of the diffuse photon wave incident on the absorber as d increases, and is similar to the effect of a fixed sized block in any optical medium – as the block moves away from a point source, the amount of blockage decreases. This effect is noticeable when the point source is scanned and a single large area detector is sensing the transmitted intensity. Figure 7(c) shows the line profiles of PD processing on Side B which indicate that contrast is best when the absorber is closest to Side B and quickly worsens as the absorber moves toward Side A. This is opposite of Fig. 7(a) and is due to the pixelated detector being able to resolve the absorber better when there is less scattering material in between the absorber and detector. There is also more noise in the PD line profiles than the LAD line profiles because the stochastic nature of the simulations is integrated over 160 pixel samples in the LAD line profiles and the integration is only over 40 source locations, which do not all overlap, in the PD line profiles. A summary of the contrast comparison between LAD and PD processing, shown in the red and blue lines of Fig. 8, leads to LAD being the preferred processing method.

A single LAD line scan is compared from the first digital phantom with no glass slides and the second digital phantom with glass slides and an air gap in Fig. 9. The glass slides and air gap slightly broaden the signature of the line scan which indicates that experimental results may appear to have worse resolution than the simulated results. There is only a single absorber in the models and experiments, so this broadening due to the experimental setup does not affect the contrast calculation since it is based on the center of the absorber and the

#201719 - $15.00 USD Received 20 Nov 2013; revised 17 Mar 2014; accepted 27 Mar 2014; published 9 Apr 2014

edges of the measurement area. There is also an absolute transmission loss due to surface reflections from refractive index mismatches. When comparing models and experiments with multiple absorbers, however, it is important to make sure the glass slides and air gap from experiments are accurately modelled in the Monte Carlo simulations.

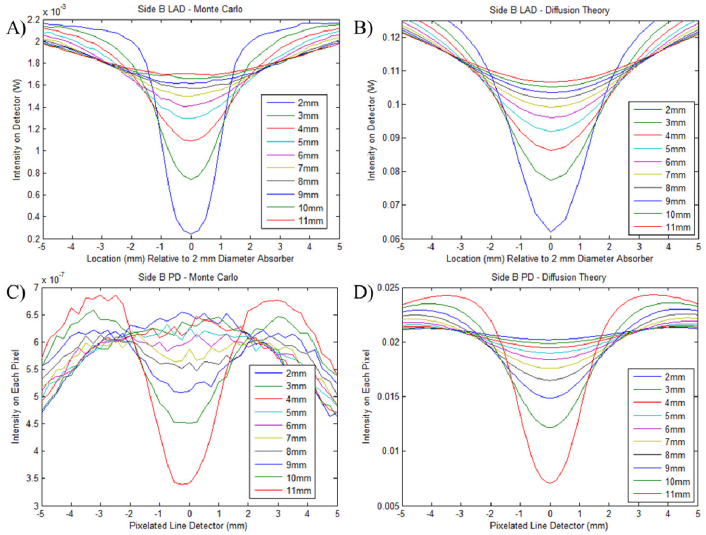

Fig. 7. Individual line profiles for absorber at different depths used to calculate contrast for (a) LAD on Side B from Monte Carlo simulations, (b) LAD on Side B from theory, (c) PD on Side B from Monte Carlo simulations, and (c) PD on Side B from diffusion theory.

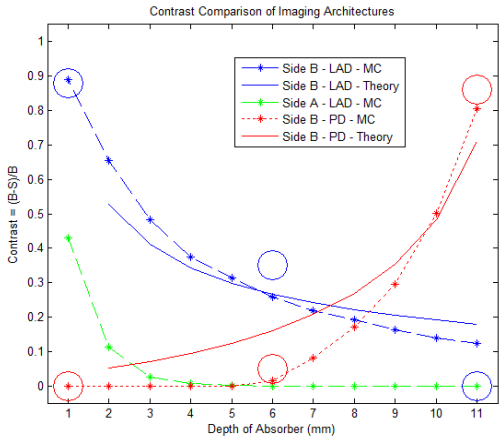

Fig. 8. Contrast comparison of system configurations, combining results from theory (solid lines), Monte Carlo (dashed lines), and experiments (large circles).

#201719 - $15.00 USD Received 20 Nov 2013; revised 17 Mar 2014; accepted 27 Mar 2014; published 9 Apr 2014

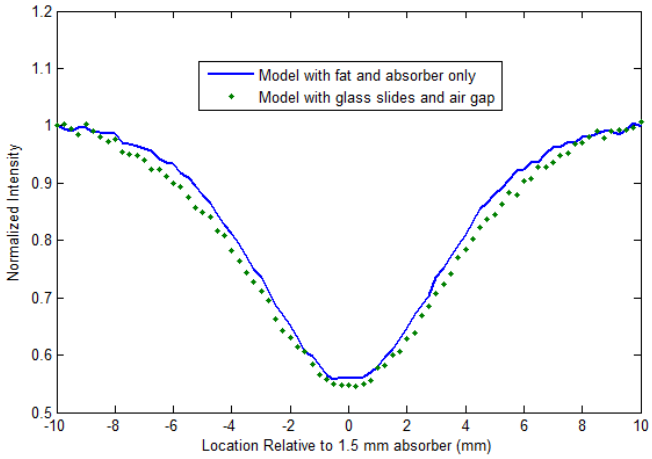

Fig. 9. Line scan for a digital phantom of 12mm of fat with absorber embedded in center compared to line scan for two 6mm digital phantoms of fat with glass slides and air gap as is the case in the experiments. Transmission configuration with LAD.

3.2 Experimental results

Sample preparation is critical for obtaining repeatable experimental results. As discussed previously, the fat samples were frozen and thawed prior to imaging which causes the solid and liquid portions (blood and interstitial fluids) to separate. The solid portion has a slippery texture similar to a raw oyster, but with more elasticity and more density. The bottom sample slide must be flat so that the liquid portions do not flow over the edges of the slide. Also, the top slide must be parallel to the bottom slide so that no lateral force causes the fat sample to move. As temperature of the sample changes the viscous forces between the liquid and solid of the fat sample interact differently, therefore imaging of a single sample (controls and all three absorber locations) is completed in a 20 minute window after the sample has warmed to room temperature. To ensure that the sample is not disturbed between imaging at each absorber location, the absorber is placed in between the two fat samples initially and then removed to capture a control image. After the control image, the absorber is place on top and bottom of the fat sample stack with low risk of disturbing the sample.

Single line scans over fat samples are difficult to interpret due to the heterogeneities in the fat tissue, so control images and scans were taken without an absorber in the sample to help normalize the heterogeneities. This normalization is helpful to identify the absorber in experiments where it is possible to capture control images, but in clinical use, normalization with a control sample is impossible. When the absorber is located on the camera side of the fat sample PD processing shows the absorber clearly, and when the absorber is located on the laser side of the fat sample LAD processing shows the absorber clearly, as expected based on simulations. When the absorber is located in the middle of the sample, neither PD or LAD processing shows the absorber clearly in a single line scan. The main reason for this is that heterogeneities in the fat sample can show the same signature as the absorber in a single line profile.

Multiple line scans improve the ability to locate an absorber of known shape with LAD processing when in the middle of the fat sample. PD processing of a four-line manual scan using Lab Setup #1 in Fig. 10(g) shows how difficult it is to detect an absorber in the middle of the fat sample. Figure 10(k) shows that detection is possible with LAD processing of multiple scan lines. If only one of the scan line profiles is viewed, there are several potential locations for an absorber and it is unclear if there is an absorber or just heterogeneities. By viewing all four line profiles simultaneously, it is clear that there is a vertical bar absorber in the fat sample.

#201719 - $15.00 USD Received 20 Nov 2013; revised 17 Mar 2014; accepted 27 Mar 2014; published 9 Apr 2014

Control images in Figs. 10(e) and 10(i) exhibit heterogeneities as seen through PD and LAD processing respectively. When the absorber is on the camera side, PD processing is effective for locating the absorber in Fig. 10(f), but LAD processing is ineffective, see Fig. 10(j). Alternatively, when the absorber is on the laser side, PD processing is ineffective in Fig. 10(h), but LAD processing is effective, see Fig. 10(l).

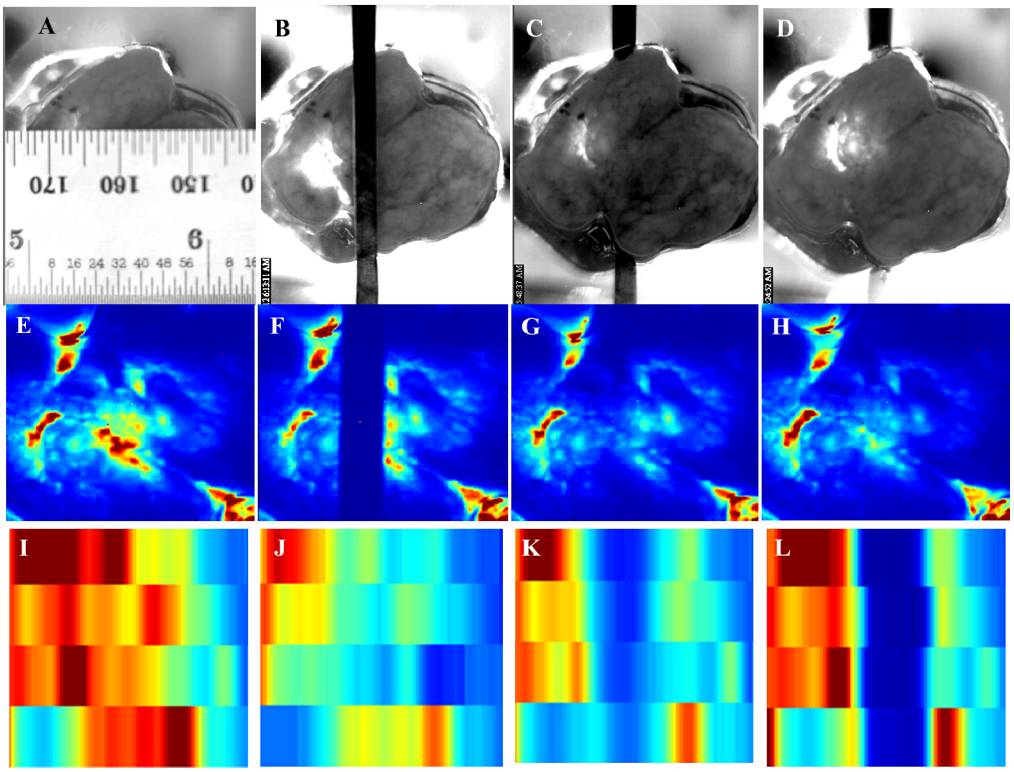

Fig. 10. Sample images from Lab Setup #1 showing (a) the size of the fat sample; a single scan location snapshot with the absorber on the (b) camera side, (c) middle, and (d) laser side; the PD processing sum of all scan locations with (e) no absorber, (f) camera side absorber, (g) middle absorber, and (h) laser side absorber; and the LAD processing scans with (i) no absorber, (j) camera side absorber, (k) middle absorber, and (l) laser side absorber.

Calculation of contrast from the experimental sample images is not as straightforward as for the simulated data due to heterogeneity. An average contrast based on *a priori* knowledge of the absorber location is calculated and displayed as large open circles in Fig. 8. The data points do not overlay directly on the simulation result lines because of noise in the experimental source and detector that are not modeled in the simulation.

It is anticipated that higher density scanning would improve the ability to detect absorbers with LAD processing, so additional fat samples are analyzed using Lab Setup #2. The 3 mm wide bar absorber is placed on the camera side of a fat sample, similar to Fig. 10(j). The scan mirror is programmed to raster scan over a 6 mm x 8 mm field of view, and photodiode sampling occurs such that the resulting image is 500 x 500 pixels. Figures 11(b) and 11(d) compared to Figs. 11(a) and 11(c) show that the bar absorber can be detected with better resolution than previously shown when the scan density is higher. There is still source and detector noise and sample heterogeneity in the LAD images that may require additional signal processing or source modulation to remove.

#201719 - $15.00 USD Received 20 Nov 2013; revised 17 Mar 2014; accepted 27 Mar 2014; published 9 Apr 2014

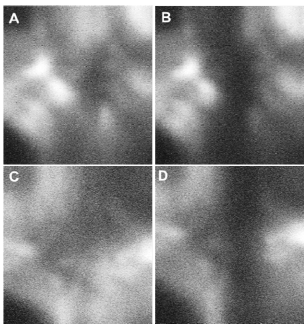

Fig. 11. Sample images from Lab Setup #2 showing (a,c) control samples with no absorber, and (b,d) samples with absorber placed on the detector side of the fat sample.

4. Conclusions

Among the system configurations evaluated, a transmission optical architecture consisting of a scanned narrow beam source and a single large area detector is preferred for detecting absorbers embedded in scattering media. Theoretical analysis of the diffusion approximation applied to a two-section scattering block with an aperture plane between the two sections is shown to be nearly identical to the diffusion approximation in a single section scattering block. The two-section theoretical analysis is also shown to be similar to Monte Carlo simulations when a bar absorber is placed in the aperture plane. Both the Monte Carlo simulations and the theoretical analysis indicate that contrast of an absorbing bar relative to surrounding scattering media is best when the bar is close to whichever source or detector has the most spatial resolution. When the source is scanned the bar has most contrast near the source, and when the detector is pixelated the bar has most contrast near the detector. When the bar is in the middle of the scattering block, equidistant from the source and detector, more contrast is seen when the source is scanned rather than when the detector is pixelated. A combination of scanned source and pixelated detector should, therefore, show the most contrast. Implementation of this architecture, however, is expensive and may not be practical to integrate into a laparoscope.

Experimentation with *ex-vivo* human fat samples imaged by an optical bench setup of the scanned source transmission configuration reveals additional challenges of imaging through fat tissue. The models and simulations assumed homogenous scattering blocks with single absorbers, but real fat samples have heterogeneities that have different scattering and absorption properties from the fat. These heterogeneities make detection of an absorbing rod more difficult, especially when the scanning area or density is low and the absorber is embedded deep in a block of fat tissue. The absorbing bar is easily identified when control images are captured without an absorbing bar; however, in practice a clinical instrument will not have such control images. Therefore, an additional method to improve contrast amongst heterogeneities should be considered.

The source wavelength should be chosen such that it is absorbed much more by the embedded structure than the surrounding media and that it is predominantly forward scattered in the surrounding media. While the results presented in this paper discuss only a monochromatic source, additional contrast and resolution improvements may be attained by switching to a multiple wavelength source in which the wavelengths are multiplexed in either time or space. Additionally, *ex-vivo* and *in-vivo* tissue optical properties are not identical, but the minor differences should not change the qualitative comparison of optical system configurations for *in-vivo* implementation.

Acknowledgments

We would like to thank Dr. Edward Livingston, M.D. and Teresa Eversole for helping access fat samples from UTSW.

#201719 - $15.00 USD Received 20 Nov 2013; revised 17 Mar 2014; accepted 27 Mar 2014; published 9 Apr 2014